Prediction of the Error Induced by Topography in Satellite Microwave Radiometric Observations

Luca Pulvirenti, *Member, IEEE*, Nazzareno Pierdicca, *Member, IEEE*, and Frank Silvio Marzano, *Senior Member, IEEE*

***Abstract*—A numerical simulator of satellite microwave radiometric observations of mountainous scenes, developed in a previous study, has been used to predict the relief effects on the measurements of a spaceborne radiometer. For this purpose, the trends of the error due to topography, i.e., the difference between the antenna temperature calculated for a topographically variable surface and that computed for a flat terrain versus the parameters representing the relief, have been analyzed. The analysis has been mainly performed for a mountainous area in the Alps by assuming a simplified land-cover scenario consisting of bare terrain with two roughness conditions (smooth and rough soils) and considering L- and C-bands, i.e., those most suitable for soil moisture retrieval. The results have revealed that the error in satellite microwave radiometric observations is particularly correlated to the mean values of the height and slope of the radiometric pixel, as well as to the standard deviations of the aspect angle and local incidence angle. Both a regression analysis and a neural-network approach have been applied to estimate the error as a function of the parameters representing the relief, using the simulator to build training and test sets. The prediction of the topography effects and their correction in radiometric images have turned out to be feasible, at least for the scenarios considered in this study.**

***Index Terms*—Microwave radiometry, relief, soil moisture, topography.**

I. Introduction

MICROWAVE radiometry of land should carefully account for large-scale relief effects when applied to hilly or mountainous areas [1], which represent important targets within earth remote sensing from satellites, particularly for hydrological purposes. Indeed, variations in topography influence the upwelling brightness temperature (T_B) measured by a satellite radiometer in several ways. The optical depth of the atmosphere is modified, the radiometer observation angle becomes a function of the surface slope, parts of the scene may be shadowed, radiation can be reflected from one tilted surface to another, and a depolarization effect occurs. Moreover, at microwave frequencies, the large variability of the mountainous scenario should be considered, if compared with the relatively large antenna footprint [2].

Manuscript received July 1, 2010; revised October 19, 2010; accepted November 16, 2010. Date of publication January 6, 2011; date of current version August 26, 2011.

The authors are with the Department of Information Engineering, Electronics and Telecommunications, Sapienza University of Rome, 00184 Rome, Italy (e-mail: pulvirenti@die.uniroma1.it; pierdicca@die.uniroma1.it; marzano@die.uniroma1.it).

Color versions of one or more of the figures in this paper are available online at http://ieeexplore.ieee.org.

Digital Object Identifier 10.1109/TGRS.2010.2096514

The effects listed earlier should be accounted for and, possibly, corrected or at least mitigated in order to remotely sensing biogeophysical parameters, such as soil moisture. Indeed, algorithms for retrieving soil moisture from spaceborne microwave radiometers (e.g., [3] and [4]) assume a relatively flat terrain, so that, as stated in [5], their application to areas with a heterogeneous surface elevation can produce significant discrepancies between estimated and actual values of this parameter.

Previous research focused on the quantification of the topography effects on microwave radiometry over land. Mätzler and Standley [1] underlined the effects resulting from the shadowing of sky radiation by an elevated horizon, as well as those due to the variable atmospheric contributions. An incentive to study the impact of the relief on the microwave radiometer measurements was given by the recent design of satellite missions dedicated to soil moisture estimation over a global scale, such as the Soil Moisture and Ocean Salinity (SMOS) one and the future Soil Moisture Active–Passive (SMAP) mission. Within the framework of the SMOS mission, the difference between the modeled T_B in the areas of complex topography and those obtained for a flat surface was highlighted in [6], while in [7], the relief was accounted for in an end-to-end performance simulator, leading to a warning on its possible impact. In [8], an approach to predict the impact of topography on microwave emission, in which the surface was replaced by the probability density function of the surface slopes, was proposed. In [9], a method to single out SMOS pixels affected by radiometric errors induced by relief, possibly hampering soil moisture retrieval, was designed. It must be noted that, as claimed in [5], topography influences also the amount of solar radiation received, having an impact on soil moisture, temperature conditions and vegetation, thus affecting surface microwave emission.

In a previous paper [10], we developed a simulator of satellite microwave radiometric observations of mountainous scenes, named Simulator of Topographic Artefacts in MIcrowave RAdiometry (STAMIRA), able to operate at different frequencies and observation angles. This simulator allowed us to carry out an analysis aiming at a complete evaluation of the error in satellite microwave radiometric imaging of a terrain with a complex relief that accounted also for the downwelling radiation scattered by the surface originated either from the sky or an elevated landscape (depending on the horizon).

Quantifying the effect of the topography can be important, for soil moisture applications, in order to flag the radiometric measurements [9]. However, if we were able not only to quantify the impact of the relief but also to predict it, we could in

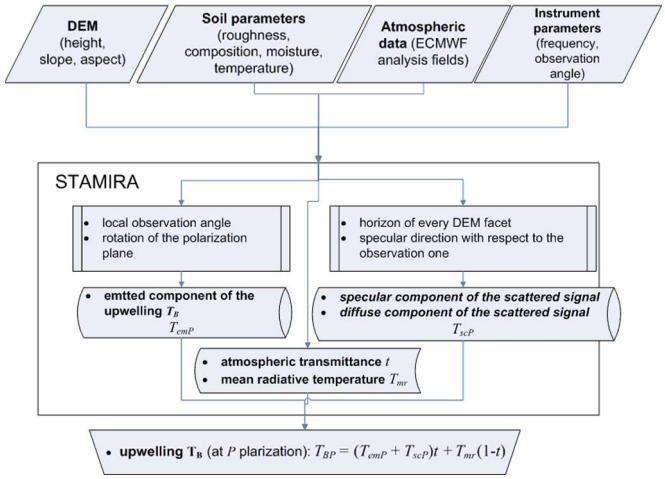

Fig. 1. Block diagram of the STAMIRA simulator.

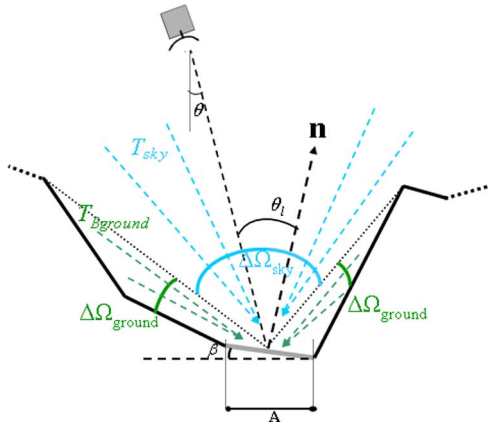

Fig. 2. Scheme of the vertical profile of the terrain assumed by STAMIRA.

principle correct unreliable data, thus retrieving soil moisture in flagged radiometric pixels too. Such a prediction, which is the objective of the present study, represents a novel contribution with respect to current literature, as well as the development of the study accomplished in [10].

In this paper, the trends of the difference between the antenna temperature calculated for a mountainous scene and that computed for a flat terrain versus the parameters representing the topography, such as local observation angle, slope, aspect, and height, are analyzed. From this analysis, an attempt to establish a relationship between the T_B variations due to relief and the aforementioned parameters is performed by applying both regression and neural-network (NN) approaches. To train the prediction algorithms, as well as to assess their results, the STAMIRA simulator has been run by employing a digital elevation model (DEM) of northern Italy, including the Alpine region. A test has been also performed for the Pyrenees. L- and C-frequency bands, i.e., those most suitable for soil moisture retrieval, have been considered for this application, and two radiometer configurations characterized by a conical scan have been assumed.

In Section II, an overview of the STAMIRA simulator is provided. Section III analyzes the correlation between the error induced by topography and the parameters representing the relief, while Section IV is dedicated to the prediction of the error. Section V draws the main conclusions.

II. Overview of the STAMIRA Simulator

The scope of this section is to resume the main equations implemented in the STAMIRA simulator; for a detailed description of its characteristics, the reader is referred to [10].

The block diagram of STAMIRA is shown in Fig. 1. STAMIRA provides the numerical simulation of a radiometric observation of a mountainous area basing on the following relationship:

$$T_{BP} = T_{emP}t + T_{scP}t + T_{mr}(1-t) \quad (1)$$

where T_{BP} is the P-polarized upwelling brightness temperature measured by a satellite radiometer (P may be H, i.e., horizontal, or V, i.e., vertical). The addends at the second member of (1) represent the various contributions to T_{BP}. The first addend is the product between the emitted component evaluated at the bottom of the atmosphere T_{emP} and the atmospheric transmittance t, whereas the second addend T_{scP} is the scattered component of the downwelling radiation, if present. The third term represents the atmospheric upwelling T_B (note that the upwelling mean radiative temperature T_{mr} has been supposed equal to the downwelling one).

A simplified scheme of a vertical section of the terrain assumed by STAMIRA to simulate T_{BP} is shown in Fig. 2, in which β is the surface slope, θ is the radiometer observation angle, and θ_l is the local observation angle. The other quantities reported in Fig. 2 will be introduced hereafter. STAMIRA includes a module for the computation of T_{emP} (see Fig. 1) that is based on the study carried out in [2]. For each DEM element, this module derives the local observation angle θ_l and the rotation angle of the polarization plane. To compute the emissivity of a facet of the DEM as a function of θ_l, STAMIRA uses the following semiempirical relationship [11]–[14]:

$$e_P(\theta_l) = 1 - \left[\Gamma_P^{sp}(\theta_l)(1-q_s) - q_s\Gamma_Q^{sp}(\theta_l)\right]\exp(-h_s) \quad (2)$$

where e_P is the P-polarized emissivity of bare soil.

The parameters q_s, denoting the polarization coupling factor and h_s, related to the surface roughness, are evaluated according to the model developed by Wang *et al.* [12], when dealing with L- and C-bands. In (2), the P- and Q-polarized (either H or V) specular Fresnel reflectivities Γ_P^{sp} and Γ_Q^{sp} (one minus the respective emissivities) are determined by applying the soil permittivity model by Dobson *et al.* [15]. The soil emissivity computed through (2) is modified to account for the polarization rotation (see [2] and [10]) and then multiplied by the soil temperature to derive T_{emP}.

As for the scattered component of the downwelling radiation, it must be firstly considered that, in the presence of relief, each surface element may diffuse both sky radiation and the radiation from the elevated landscape, depending on the local horizon (see Fig. 2). To calculate T_{scP}, STAMIRA describes

the surface bistatic scattering behavior at P-polarization as a combination of a specular coherent component and a term representing the diffuse incoherent component. Basing on this scheme, the surface reflectivity turns out to be

$$\begin{aligned}\Gamma_P(\theta_l) &= 1 - e_P(\theta_l) \\ &= \frac{1}{4\pi\cos\theta_l}\int_{2\pi}\sigma_P^0\, d\Omega_s \\ &= (1-a_{sp})\Gamma_P^{in} + a_{sp}\Gamma_P^{sp}(\theta_l). \end{aligned} \tag{3}$$

In (3), σ_P^0 is the bistatic scattering coefficient at P-polarization, given by the sum of a copolarized component and a cross-polarized one, and a_{sp}, spanning the interval [0–1], represents the specularity factor. The term Γ_P^{in} of (3) originates from the incoherent component of the bistatic scattering coefficient. Note that, to make $\Gamma_P(\theta_l)$ consistent with the expression of $e_P(\theta_l)$ given by (2), a_{sp} and Γ_P^{in} have to be expressed as

$$a_{sp} = (1-q_s)\exp(-h_s) \tag{4a}$$

$$\Gamma_P^{in} = q_s\Gamma_Q^{sp}\exp(-h_s)/(1-a_{sp}). \tag{4b}$$

The knowledge of the coherent and incoherent components of the surface reflectivity allows expressing the downwelling brightness temperature scattered by a surface element (i.e., a facet of the DEM). STAMIRA evaluates T_{scP} as [10]

$$\begin{aligned}T_{scP} = a_{sp}\Gamma_P^{sp}T_{sp} + (1-a_{sp})\left(\Gamma_P^{in}/\pi\right) \\ \times\left[\int_{\Delta\Omega_{\text{ground}}} T_{B_{\text{ground}}}[\mathbf{n}\cdot\mathbf{m}]\, d\Omega_s \right. \\ \left. + \int_{\Delta\Omega_{sky}} T_{\text{sky}}[\mathbf{n}\cdot\mathbf{m}]\, d\Omega_s\right]\end{aligned} \tag{5}$$

where T_{sp} is the brightness temperature impinging the DEM facet from the specular direction (either from the sky or an elevated surface, depending on the horizon), while T_{sky} and T_{Bground} are the downwelling radiations coming from below and above the horizon, respectively (see Fig. 2). The term $\mathbf{n}\cdot\mathbf{m}$ is the scalar product between the versor of the surface normal and the unit vector representing the direction from which the radiation impinges on the surface. $\Delta\Omega_{\text{ground}}$ denotes the solid angle under which each individual facet observes the surrounding terrain, and $\Delta\Omega_{\text{sky}}$ is the corresponding quantity for the sky radiation T_{sky} (see Fig. 2). The latter quantity is given by

$$T_{\text{sky}} = T_{mr}(1-t) + T_{\cos}t \tag{6}$$

where $T_{\cos}$ (assumed to be equal to 2.75 K) is the cosmic background. Note that the extraterrestrial T_B has been approximated to $T_{\cos}$.

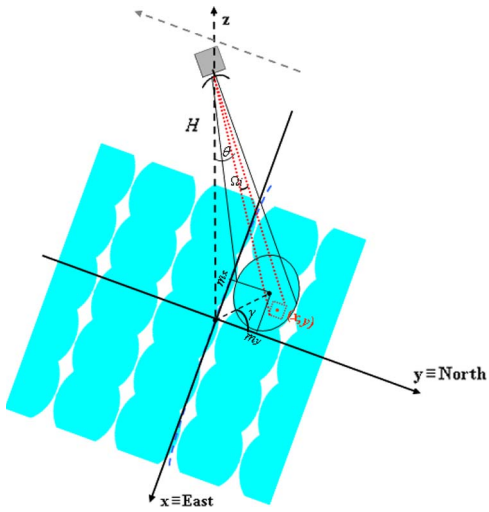

Fig. 3. Measurement geometry assumed by STAMIRA to evaluate the radiometer antenna temperature. The cyan ellipses represent the IFOVs of the radiometer antenna.

The way STAMIRA determines the specular component and evaluates the term within the square brackets in (5), which is proportional to the irradiance incident on the surface, is described in detail in [10]. Basically, a module implementing a ray-tracing algorithm is set up in order to determine the horizon of every DEM facet and to distinguish between the irradiance due to the elevated landscape [the first integral in (5)] and sky radiation (second integral).

Once the various terms of (1) are computed for each DEM cell, STAMIRA evaluates the number n of elements of the DEM comprised in every radiometric pixel, i.e., in the instantaneous field of view (IFOV) of the radiometer antenna, as described in [2]. Making reference to Fig. 3, showing the measurement geometry considered by STAMIRA that assumes a conically scanning radiometer, an element of the DEM, whose central point coordinates are (x, y), is contained in the radiometer IFOV if the following inequality is satisfied:

$$\begin{aligned}\frac{(x-m_x)^2}{\sigma_x^2} + \frac{(y-m_y)^2}{\sigma_y^2} \\ + \tan(2\gamma)\frac{(\sigma_x^2-\sigma_y^2)}{\sigma_x^2\sigma_y^2}(x-m_x)(y-m_y) \le 1.\end{aligned} \tag{7}$$

In (7), σ_x and σ_y denote the semiaxes of the ellipse representing the IFOV, while m_x and m_y are the coordinates of the IFOV center, and γ represents the azimuthal step of the scanning system.

The final evaluation of the antenna temperature, including the identification of the pixels affected by shadowing in the IFOV (that do not contribute to T_{BP}), has been carried out as in [10], where it has been assumed, for simplicity, an antenna characterized by a major lobe efficiency that is equal to one and by a constant directivity D within the major lobe. Indicating by β_i the slope angle of the ith element of the DEM included in the considered radiometric pixel, by θ_{li} its local observation angle (see Fig. 2), and by T_{BPi} its brightness temperature, expressed

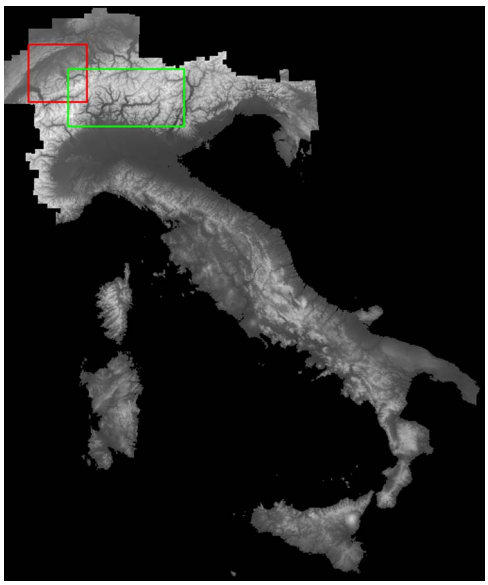

Fig. 4. DEM of Italy. The green and red boxes enclose the portions of the DEM used in this paper, both included in the Alpine region.

by (1), the antenna temperature at P polarization T_P has been estimated through the following:

$$T_P = \frac{\sum_{i=1}^{N} T_{BPi} D\Omega_i}{\sum_{i=1}^{N} D\Omega_i} = \frac{\sum_{i=1}^{N} T_{BPi} D \frac{A\cos\theta_{li}}{H^2\cos\beta_i}}{\sum_{i=1}^{N} D \frac{A\cos\theta_{li}}{H^2\cos\beta_i}} = \frac{\sum_{i=1}^{N} T_{BPi} \frac{\cos\theta_{li}}{\cos\beta_i}}{\sum_{i=1}^{N} \frac{\cos\theta_{li}}{\cos\beta_i}}. \tag{8}$$

In (8), A is the area of a DEM element referenced to a projection on the horizontal plane (see Fig. 2), so that its actual area is given by $(A/\cos\beta_i)$, while Ω_i is the solid angle under which the ith facet is observed by the radiometer (see Fig. 3) that is equal to $(A\cos\theta_{li}/H^2\cos\beta_i)$, being H the range from the DEM cell to the satellite, which has been supposed constant considering a conical scanning and neglecting the cell height with respect to the satellite height.

III. Error as a Function of the Topography Parameters

The error due to the topography is evaluated in terms of $\Delta T_P = T_P - T_{P\_\mathrm{flat}}$, which is the difference between the antenna temperature calculated through (8) and that computed for a flat terrain (having the same roughness, moisture, and composition) placed at an altitude that is equal to the average of the heights of the DEM facets within the antenna IFOV. Looking at the block diagram shown in Fig. 1, STAMIRA requires a DEM of the area of interest, the characteristics of the soil, the atmospheric data, and the instrument parameters.

A DEM of Italy, having a spatial resolution of 250 $\times$ 250 m, has been mainly used in this work. In particular, we have considered a portion of 1600 $\times$ 512 DEM elements (400×128 km^2) placed in northern Italy to focus our analysis on the Alps. The DEM is shown in Fig. 4, and the area considered in this phase of our study is highlighted in green.

As for the soil parameters, the following values have been used as inputs to STAMIRA: volumetric moisture that is equal to 0.25, dry soil density that is equal to 1.3 g/m^3, and fractions of sand and clay that are equal to 32% and 25%, respectively. Concerning the surface temperature T_s, a decrease with the height z, according to a standard temperature gradient of 6.5 K/km, has been assumed, supposing T_s at sea level $(z = 0)$ to be equal to 296 K. Note that, for the sake of simplicity, we do not account for the relation between topography and quantities influencing surface emission, such as soil moisture and temperature [5], considering also that they are related to environmental processes and not to the measurement technique. Moreover, T_s has been supposed constant with the depth in the soil over the range of penetration of the considered frequencies. The present release of STAMIRA assumes bare soil coverage, thus avoiding vegetation effects, in order to single out those due to relief. Two values of standard deviation of the surface height s, i.e., $s = 0.73$ cm (smooth soil) and $s = 2.45$ cm (rough soil), have been used. As for the atmospheric parameters, considering L- and C-bands and nonprecipitating weather conditions, the atmosphere has been approximately considered transparent [11].

Regarding the instrument parameters, for C-band, we have made reference to the Advanced Microwave Scanning Radiometer for the Earth Observing System (AMSR-E) [16], supposing a sensor operating at 6.9 GHz, observing the Earth at 55° from an altitude of 705 km and with a spatial resolution of 75×43 km^2. For L-band (1.4 GHz), we have considered an instrument characterized by an observation angle of 40°, and orbiting at 670 km of altitude, as that foreseen for the radiometer aboard the future SMAP mission [17]. A spatial resolution of 40×40 km^2 has been assumed, because the SMAP radiometer-based soil moisture product will be posted on a 36-km grid [17]. It is worth noting that worsening of the resolution tends to smooth the different contributions coming from the surface cells. Such smoothing mitigates the variability of ΔT_P, but it does not cause a considerable change of its average value because the topography affects the brightness temperature of each surface point independently of the instrument characteristics (because of polarization mixing, shadowing, and so on).

To estimate the error induced by the relief, which is the goal of this study, we have computed the mean values of height (m_h), slope (m_β), aspect (m_α), and local incidence angle $(m_{\theta l})$, of the DEM elements within the radiometric IFOV [whose number is determined through (7)], as well as the standard deviations of these parameters, denoted as σ_h, σ_β, σ_α, and $\sigma_{\theta l}$, respectively. Then, we have calculated the correlation coefficient (R) between $\Delta T_P = T_P - T_{P\_\mathrm{flat}}$ and the aforementioned variables describing the topography of the area of interest. The results, for the Alpine area, are reported in Table I (C-band) and Table II (L-band).

It can be noted that, considering m_h, m_β, $\sigma_{\theta l}$, and σ_α, the correlation coefficient is larger than 0.7 both for C- and L-bands and for the two roughness conditions (except $\sigma_{\theta l}$ for L-band, rough soil, vertical polarization). In particular, the values of R that are larger than 0.9 have been found at C-band, for m_β, σ_α, and $\sigma_{\theta l}$, while m_α and $m_{\theta l}$ are the parameters presenting the least value of R. It is worth pointing out that, for C-band, R has

TABLE I
CORRELATION COEFFICIENT (R) BETWEEN $\Delta T_P = T_P - T_{P\_\mathrm{flat}}$ AND THE RELIEF PARAMETERS FOR C-BAND. BOLD DENOTES $R \geq 0.7$. THE ALPINE AREA (RED BOX IN FIG. 4) IS CONSIDERED

	m_h	$m_{\theta l}$	m_β	m_α	σ_h	$\sigma_{\theta l}$	σ_β	σ_α
Rough H-pol.	**0.81**	0.21	**0.99**	0.01	**0.85**	**0.99**	0.63	**0.92**
Rough V-pol.	**0.87**	0.45	**0.97**	0.07	**0.83**	**0.94**	0.55	**0.95**
Smooth H-pol.	**0.85**	0.32	**0.99**	0.05	**0.85**	**0.97**	0.60	**0.94**
Smooth V-pol.	**0.87**	0.40	**0.98**	0.07	**0.84**	**0.95**	0.57	**0.94**

TABLE II
SAME AS TABLE I, BUT FOR L-BAND

	m_h	$m_{\theta l}$	m_β	m_α	σ_h	$\sigma_{\theta l}$	σ_β	σ_α
Rough H-pol.	**0.83**	0.08	**0.98**	0.16	**0.84**	**0.94**	0.59	**0.86**
Rough V-pol.	**0.77**	0.58	**0.70**	0.15	0.55	0.59	0.33	**0.77**
Smooth H-pol.	**0.86**	0.07	**0.96**	0.18	**0.82**	**0.91**	0.56	**0.88**
Smooth V-pol.	**0.84**	0.41	**0.82**	0.18	0.67	**0.73**	0.43	**0.84**

been computed considering 264 radiometric pixels, i.e., those included in the considered Alpine region of 400×128 km^2 according to the outcome of the application of (7) (note that AMSR-E has a pixel spacing of 10×10 km^2 at C-band). As for L-band, the results in Table II have been obtained by analyzing 48 pixels, having assumed a pixel spacing on the order of the dimension of the pixel itself [17].

Plots of $\Delta T_P = T_P - T_{P\_\mathrm{flat}}$ versus m_h, m_β, $\sigma_{\theta l}$, and σ_α are shown in Fig. 5, Fig. 6 (C-band), and Fig. 7 (L-band). Note that we have included in our analysis a large range of mean surface heights (see upper panels) spanning an interval of approximately 250–2600 m at both C- and L-bands. At horizontal polarization (H-pol), $\Delta T_P = T_P - T_{P\_\mathrm{flat}}$ is a positive quantity, while the opposite occurs at V-pol. As explained in [10], the downward radiation impinging on the surface is due not only to the atmospheric T_B, which is fairly low, but also to the radiation coming from surrounding surface cells placed at higher altitude (see Fig. 2). The latter radiation is quite high considering that the emissivity of the terrain is around 0.9, so that it increases the scattered component of the downwelling brightness temperature. Another important effect of the topography is the mixing of the two linearly polarized components radiated by a surface facet [2], which implies a general increase of the emitted component at H-pol, while the V-pol one tends to decrease. These two effects have different relative impact on the resulting radiometric observations, depending on the polarization. At H-pol, the increase of T_{scP}, due to the fact that the surfaces illuminated by radiation from surrounding elevated terrain enhance their T_B with respect to facets scattering atmospheric downward radiation only, is added to the increase of T_{emP}, mainly due to the polarization coupling [2], so that $T_H > T_{H\_\mathrm{flat}}$. As for V-pol, the increase of the scattered component due to the radiation of the elevated landscape does not compensate for the decrease

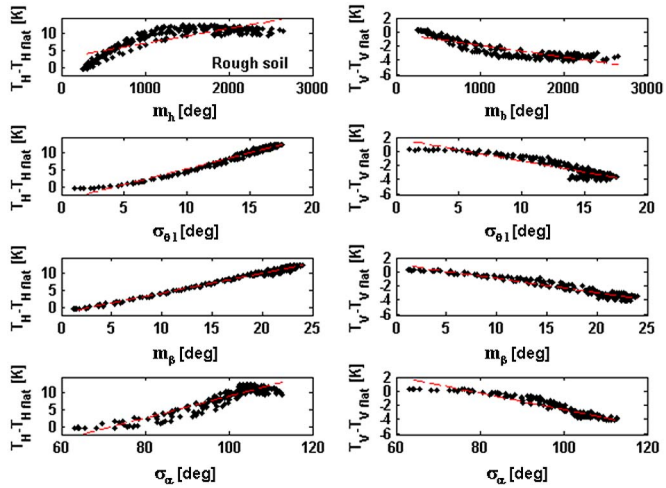

Fig. 5. $T_P - T_{P\_\mathrm{flat}}$ versus m_h, $\sigma_{\theta l}$, m_σ, and σ_α for a rough soil and C-band. The Alpine area (red box in Fig. 4) is considered. (Left panels) H polarization. (Right panels) V polarization. The red dashed line represents the best fit.

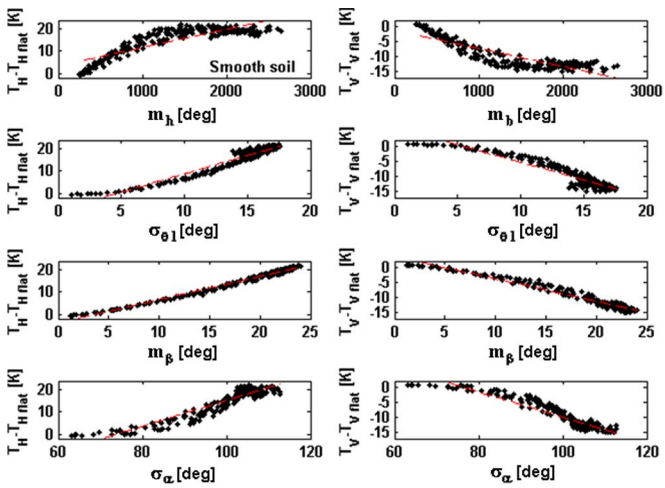

Fig. 6. Same as Fig. 5, but for a smooth soil.

of the emitted component, so that $T_V - T_{V\_\mathrm{flat}} < 0$ [10]. Note that from the study accomplished in [18] for L-band, it emerged that $T_V < T_{V\_\mathrm{flat}}$ and $T_H > T_{H\_\mathrm{flat}}$ because of the topography, in agreement with our findings.

Figs. 5–7 confirm the correlation between m_h, m_β, $\sigma_{\theta l}$, σ_α, and the error induced by the relief. To emphasize the increase of $\Delta T_H = T_H - T_{H\_\mathrm{flat}}$ with the increase of these topography parameters and the opposite behavior of $\Delta T_V = T_V - T_{V\_\mathrm{flat}}$, the best fit line is also reported (in red). Note that the trend of ΔT_P versus m_h, m_β, $\sigma_{\theta l}$, and σ_α at L-band for a rough soil is quite similar to that shown in Fig. 7. The corresponding plots are therefore omitted for conciseness.

The results shown in Figs. 5–7 and those reported in Tables I and II indicate that, at least for the simplified land-cover scenario considered here, in which homogeneous characteristics of the observed surface (i.e., bare soil with uniform moisture and roughness) are assumed, it is possible to predict the error made by observing a mountainous area through a spaceborne microwave radiometer, so that a correction of this error can be envisaged.

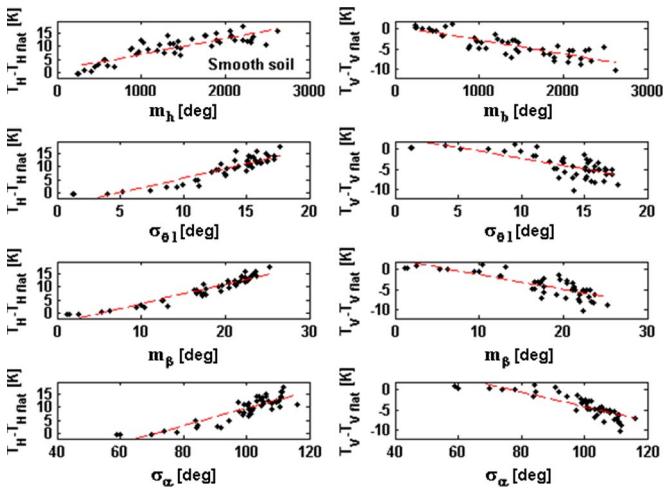

Fig. 7. Same as Fig. 6, but for L-band.

IV. Prediction of the Error Due to Relief

To evaluate the error related to topography, on the basis of the eight parameters introduced in the previous section, we have considered both a regression analysis (RA) and an NN approach, as we have profitably done in previous works for both direct and inverse problems (e.g., [19]–[21]).

We have simulated eight different experiments, trying to predict ΔT_P using the topographic parameters at two polarizations, two frequency bands, and two roughness conditions of the bare surface. We have built eight databases consisting of either 264 (C-band) or 48 (L-band) vectors, each containing the values of m_h, m_β, m_α, $m_{\theta l}$, σ_h, σ_β, σ_α, and $\sigma_{\theta l}$, coupled to the STAMIRA-derived ΔT_P.

First of all, we have verified the utility to employ all the topographic parameters as predictors of ΔT_P. On one hand, we have shown in the previous section that some of these parameters presented quite small values of R, although in principle they might carry information on the error. On the other hand, the quantities that turned out to be correlated with ΔT_P might be also strictly correlated to each other, being derived from the same DEM, thus carrying the same information. A principal component analysis is suitable to reduce the dimensionality of a data set by decreasing the number of variables without losing the information content.

We have applied the RA to the new databases obtained by transforming the original ones into the space of the principal components. To this aim, the new databases have been divided in training and test sets through a systematic sampling, as we have done in [19] and [22]. The coefficients of the regressions found from the RA of the training sets have been used to predict, for the test sets, the STAMIRA-derived values of $\Delta T_P = T_P - T_{P\_\mathrm{flat}}$. Tables III and IV report the values of the root mean square (rms) difference between STAMIRA-derived and predicted ΔT_P values that we have found, for the test sets, by varying the number of the principal components (N_{PC}).

Tables III and IV suggest that each principal component generally adds information on the error ΔT_P. It can be also noted that, for L-band V-pol, using four or seven components results in the same rms difference between STAMIRA and predicted

TABLE III
Values (in Kelvin) of the rms Difference Between STAMIRA-Derived and Predicted $\Delta T_P = T_P - T_{P\_\mathrm{flat}}$'s for the First Test Set Considered in This Paper (132 Records; Red Box in Fig. 4) at C-Band

	$N_{PC}=4$	$N_{PC}=5$	$N_{PC}=6$	$N_{PC}=7$	$N_{PC}=8$
Rough H-pol.	0.66	0.64	0.29	0.21	0.21
Rough V-pol.	0.24	0.23	0.15	0.14	0.11
Smooth H-pol.	1.16	1.13	0.66	0.54	0.37
Smooth V-pol.	0.87	0.85	0.54	0.48	0.34

TABLE IV
Same as Table III, but for L-Band (24 Records)

	$N_{PC}=4$	$N_{PC}=5$	$N_{PC}=6$	$N_{PC}=7$	$N_{PC}=8$
Rough H-pol.	0.97	0.98	0.79	0.70	0.59
Rough V-pol.	0.41	0.41	0.41	0.41	0.21
Smooth H-pol.	1.36	1.36	1.24	1.16	0.76
Smooth V-pol.	0.87	0.87	0.87	0.87	0.41

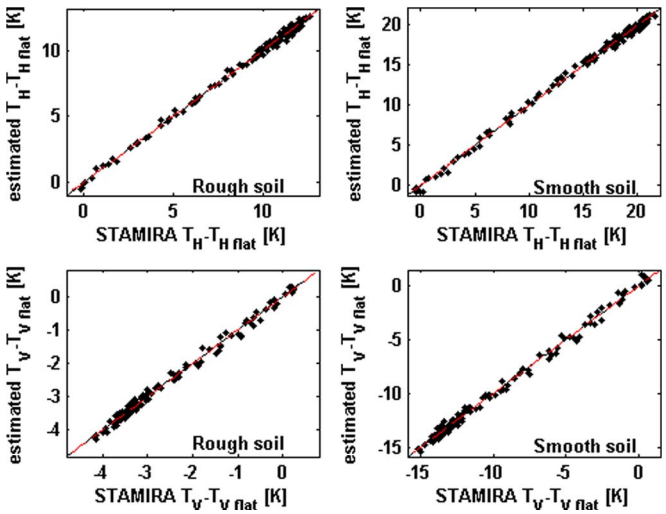

Fig. 8. Predicted through the regression approach versus STAMIRA $\Delta T_P = T_P - T_{P\_\mathrm{flat}}$ for the first test set considered in this paper (132 records; red box in Fig. 4) at C-band. The red dashed line denotes the best fit. The black line indicates perfect agreement.

errors, while the quality of the estimates improves using all the eight components, i.e., considering all the parameters representing the topography $(m_h, m_\beta, m_\alpha, m_{\theta l}, \sigma_h, \sigma_\beta, \sigma_\alpha,$ and $\sigma_{\theta l})$ as predictors. We have also found that the correlation coefficient between estimated and simulated ΔT_P's is always larger than 0.94 even for $N_{\mathrm{PC}} = 4$.

The previous finding has led us to use all the parameters that we have chosen to represent the topography of the area of interest as predictors. The results of the application of the regression approach by employing all the predictors are shown in Fig. 8 (C-band) and Fig. 9 (L-band), whereas the corresponding values of rms difference between the predicted and STAMIRA ΔT_P's can be read in the sixth column of Tables III and IV. The results of the regression are worse for L-band with respect to C-band mainly because of the less number of records of the training set (24, i.e., 48/2, having split the STAMIRA-derived databases in the training and test ones, versus 132, i.e., 264/2). Although the inherent low resolution of a microwave radiometer implies that a small number of pixels cover the

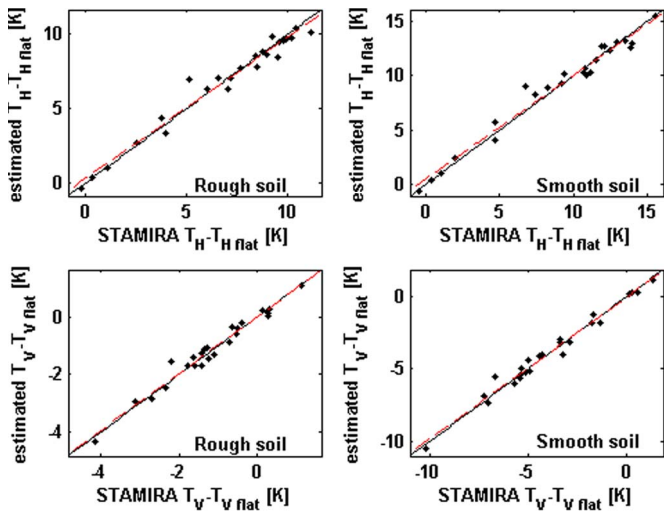

Fig. 9. Same as Fig. 8, but for L-band (24 records).

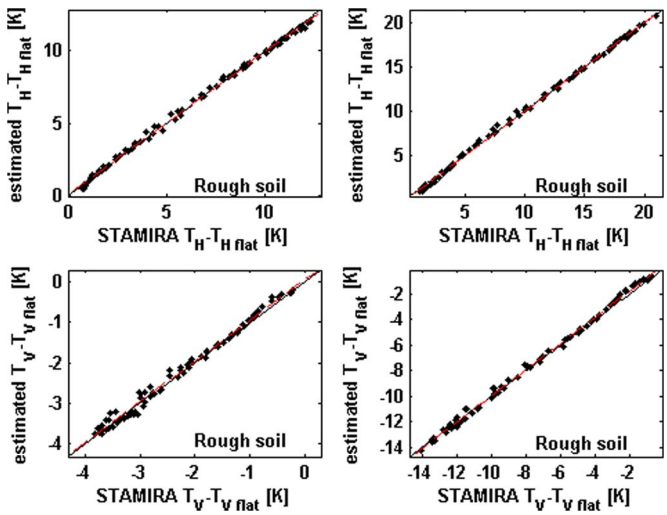

Fig. 10. Predicted through the NN approach versus STAMIRA $\Delta T_P = T_P - T_{P\_\mathrm{flat}}$ for the second test set considered in this paper (green box in Fig. 4) at C-band. The red dashed line denotes the best fit. The black line indicates perfect agreement.

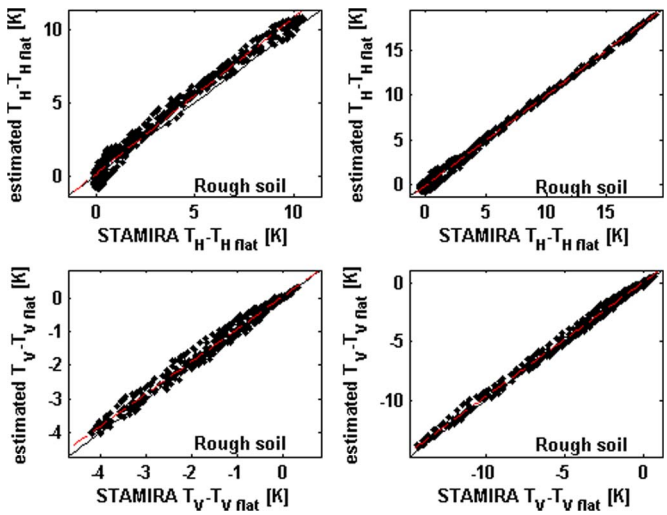

Fig. 11. Predicted through the NN approach versus STAMIRA $\Delta T_P = T_P - T_{P\_\mathrm{flat}}$ for the third test set considered in this paper at C-band (Pyrenees). The red dashed line denotes the best fit. The black line indicates perfect agreement.

Alpine region (particularly at L-band for which such a poor resolution is combined to a large pixel spacing), thus limiting the dimension of the training sets, the results seem to indicate the feasibility of the proposed method to estimate the error due to topography. Note that further widening of the selected Alpine area would have added only few pixels to the training set without substantially changing the results.

As for the NN approach, we have chosen an architecture consisting of eight input neurons (i.e., the number of predictors), eight hidden neurons, and four outputs (two polarizations times two soil conditions). Two different networks have been designed for C- and L-bands. Regarding the learning algorithm, we have chosen the Bayesian regularization, in combination with the Levenberg–Marquardt training, as done in [19] and [21]. Such a choice allows a high efficiency and ensures the capability of a NN to properly respond to unexpected inputs (i.e., the so-called generalization). The latter feature can be important when dealing with a highly variable topography such as that characteristic of the Alpine region.

The outcomes obtained by applying the NN approach to the same training and test sets used for RA have turned out to be substantially the same for L-band, while an improvement has been found for C-band. Again, this different behavior can be mainly ascribed to the small dimension of the L-band training set, on its turn related to the pixel spacing that we have assumed to simulate the SMAP measurements, which might not ensure an optimal NN training. We have obtained the following values of rms difference between the predicted and STAMIRA ΔT_P's at C-band: 0.10 K (rough soil, H-pol), 0.10 K (rough soil, V-pol), 0.03 K (smooth soil, H-pol), and 0.06 K (smooth soil, V-pol). These values have to be compared with those reported on the sixth column of Table III.

Two further tests have been carried out for C-band to verify whether the proposed approach could represent a reliable road to predict the relief effects. We have considered, as test sets, both a different Alpine area (red box in Fig. 4), only partially overlapping the previous one, and another geographic region, that is the Pyrenees, taking advantage of the availability of a DEM of the Pyrenean chain (250 $\times$ 250 m of resolution). We have run STAMIRA for these new DEMs too (512 $\times$ 512 pixels for the Alpine DEM; 1500 $\times$ 500 pixels for the Pyrenean one). For this exercise, all the 264 values of $\Delta T_P = T_P - T_{P\_\mathrm{flat}}$ derived from the DEM that was previously used have been included in the training set. The aim of this final part of our study is the evaluation of the outcomes for test sets that are totally independent from the training one, exploiting the existence of a certain degree of spatial coherence between the topographic structures in the Alps and the Pyrenees [5]. The results of these tests are shown in Figs. 10 and 11 for the NN approach, whereas Table V reports the rms difference between STAMIRA and predicted ΔT_P's for both the algorithms.

Looking at Figs. 10 and 11 the encouraging results obtained in the previous test of the proposed methodology are confirmed. Looking at Table V, the difference between the

TABLE V
VALUES (IN KELVIN) OF THE RMS DIFFERENCE BETWEEN STAMIRA-DERIVED AND PREDICTED $\Delta T_P = T_P - T_{P\_\mathrm{flat}}$'s AT C-BAND. THE VALUES IN THE FIRST TWO ROWS REGARD THE SECOND TEST SET CONSIDERED IN THIS PAPER (GREEN BOX IN FIG. 4). THE VALUES IN THE LAST TWO ROWS CONCERN THE THIRD TEST SET (PYRENEES)

	Rough H-pol.	Rough V-pol.	Smooth H-pol.	Smooth V-pol.
NN	0.18	0.23	0.12	0.25
RA	0.34	0.29	1.93	1.61
NN	0.70	0.43	0.17	0.37
RA	0.87	0.30	2.15	1.07

performances yielded by the algorithms for smooth soils is evident. In this case, the improvement achieved by using the NN can be ascribed to the generalization capability of the Bayesian regularization learning that allows dealing with a different area of interest. We have found that the worse behavior of RA with respect to NN is particularly evident in the range of small $|\Delta T_P|$, probably because the first data set used in this work (employed as training set for these final tests) includes a large number of records with high $|\Delta T_P|$ (see Fig. 8).

It must be finally underlined that, although an NN trained for the Alps has yielded fairly good performances for the Pyrenees as well, we do not claim that, once the NN (or a regression) is trained on a specific region, it can be used worldwide. Indeed, taking advantage of the availability of elevation data on a near-global scale (e.g., through the Shuttle Radar Topography Mission), the simulator can be run in any geographic area of interest (or at least in a representative sample of it) to produce a reliable training set.

V. CONCLUSION

A numerical simulator of satellite microwave radiometric observations of mountainous scenes has been used to assess the feasibility of predicting the relief effects on the measurements of a spaceborne microwave radiometer. For this purpose, the trends of the difference between the antenna temperature computed for a surface with complex topography and that calculated for a flat terrain versus the parameters describing the relief have been analyzed. To represent the relief, we have selected quantities that can be derived from a DEM, such as the mean values and standard deviations, within the radiometer antenna footprint, of height, slope, aspect, and local incidence angle. The study has been mainly performed making reference to a mountainous area in the Alps and considering two conically scanning instruments operating at L- and C-bands.

The results have shown the strict correlation existing between the error in satellite microwave radiometric observations due to relief and some of the parameters previously listed. A regression analysis and a neural-network approach have been used to estimate this error as a function of the parameters representing the relief, yielding encouraging results. Although the proposed methodology needs to be validated for more complex scenarios that should include, for instance, a heterogeneous surface with variable moisture and roughness, as well as vegetation cover, it seems to represent a valid road to tackle the problem of modeling and correcting the effects due to topography in problems concerning the retrieval of biogeophysical parameters, such as soil moisture, from microwave radiometric data.

REFERENCES

[1] C. Mätzler and A. Standley, "Technical note: Relief effects for passive microwave remote sensing," *Int. J. Remote Sens.*, vol. 21, no. 12, pp. 2403–2412, Aug. 2000.

[2] L. Pulvirenti, N. Pierdicca, and F. S. Marzano, "Topographic effects on the surface emissivity of a mountainous area observed by a spaceborne microwave radiometer," *Sensors*, vol. 8, no. 3, pp. 1459–1474, Mar. 2008.

[3] W. T. Crow, M. Drusch, and E. F. Wood, "An observation system simulation experiment for the impact of land surface heterogeneity on AMSR-E soil moisture retrieval," *IEEE Trans. Geosci. Remote Sens.*, vol. 38, no. 8, pp. 1622–1631, Aug. 2001.

[4] I. J. Davenport, J. Fernandez-Galvez, and R. J. Gurney, "A sensitivity analysis of soil moisture retrieval from the tau–omega microwave emission model," *IEEE Trans. Geosci. Remote Sens.*, vol. 43, no. 6, pp. 1304–1316, Jun. 2005.

[5] A. N. Flores, V. Y. Ivanov, D. Entekhabi, and R. L. Bras, "Impact of hillslope-scale organization of topography, soil moisture, soil temperature, and vegetation on modeling surface microwave radiation emission," *IEEE Trans. Geosci. Remote Sens.*, vol. 47, no. 8, pp. 2557–2571, Aug. 2009.

[6] Y. H. Kerr, F. Secherre, J. Lastenet, and J. P. Wigneron, "SMOS: Analysis of perturbing effects over land surfaces," in *Proc. IEEE IGARSS*, Jul. 2003, vol. 2, pp. 908–910.

[7] M. Talone, A. Camps, A. Monerris, M. Vall-Ilossera, P. Ferrazzoli, and M. Piles, "Surface topography and mixed-pixel effects on the simulated L-band brightness temperatures," *IEEE Trans. Geosci. Remote Sens.*, vol. 45, no. 7, pp. 1996–2003, Jul. 2007.

[8] C. Utku and D. M. Le Vine, "A model for prediction of the impact of topography on microwave emission," *IEEE Trans. Geosci. Remote Sens.*, vol. 49, no. 1, pp. 395–405, Jan. 2011.

[9] A. Mialon, L. Coret, Y. H. Kerr, F. Secherre, and J.-P. Wigneron, "Flagging the topographic impact on the SMOS signal," *IEEE Trans. Geosci. Remote Sens.*, vol. 46, no. 3, pp. 689–694, Mar. 2008.

[10] N. Pierdicca, L. Pulvirenti, and F. S. Marzano, "Simulating topographic effects on spaceborne radiometric observations between L and X frequency bands," *IEEE Trans. Geosci. Remote Sens.*, vol. 48, no. 1, pp. 273–282, Jan. 2010.

[11] Y. H. Kerr and E. G. Njoku, "A semi empirical model for interpreting microwave emission from semiarid land surfaces as seen from space," *IEEE Trans. Geosci. Remote Sens.*, vol. 28, no. 3, pp. 384–393, May 1990.

[12] J. R. Wang, P. E. O'Neill, T. J. Jackson, and E. T. Engman, "Multifrequency measurements of the effects of soil moisture, soil texture and surface roughness," *IEEE Trans. Geosci. Remote Sens.*, vol. GRS-21, no. 1, pp. 44–51, Jan. 1983.

[13] J. R. Wang and B. J. Choudhury, "Remote sensing of soil moisture content over bare field at 1.4 GHz frequency," *J. Geophys. Res.*, vol. 86, no. C6, pp. 5277–5282, 1981.

[14] C. Prigent, J. P. Wigneron, W. B. Rossow, and J. R. Pardo-Carrion, "Frequency and angular variations of land surface microwave emissivities: Can we estimate SSM/T and AMSU emissivities from SSM/I emissivities," *IEEE Trans. Geosci. Remote Sens.*, vol. 38, no. 5, pp. 2373–2386, Sep. 2000.

[15] M. C. Dobson, F. T. Ulaby, M. T. Hallikainen, and M. El-Rayes, "Microwave dielectric behavior of wet soil—Part II: Dielectric mixing models," *IEEE Trans. Geosci. Remote Sens.*, vol. GRS-23, no. 1, pp. 35–46, Jan. 1985.

[16] T. Kawanishi, T. Sezai, Y. Ito, K. Imaoka, T. Takeshima, Y. Ishido, A. Shibata, M. Miura, H. Inahata, and R. W. Spencer, "The Advanced Microwave Scanning Radiometer for the Earth Observing System (AMSR-E), NASDA's contribution to the EOS for global energy and water cycle studies," *IEEE Trans. Geosci. Remote Sens.*, vol. 41, no. 2, pp. 184–194, Feb. 2003.

[17] D. Entekhabi, E. G. Njoku, P. E. O'Neill, K. H. Kellogg, W. T. Crow, W. N. Edelstein, J. K. Entin, S. D. Goodman, T. J. Jackson, J. Johnson, J. Kimball, J. R. Piepmeier, R. D. Koster, N. Martin, K. C. McDonald, M. Moghaddam, S. Moran, R. Reichle, J. C. Shi, M. W. Spencer, S. W. Thurman, L. Tsang, and J. Van Zyl, "The Soil Moisture Active Passive (SMAP) mission," *Proc. IEEE*, vol. 98, no. 5, pp. 704–716, May 2010.

[18] C. Utku and D. Le Vine, "Topography effects on brightness temperature in remote sensing at L-band," in *Proc. URSI GA*, Chicago, IL, Mar. 2008.
[19] L. Pulvirenti, N. Pierdicca, and F. S. Marzano, "Modeling microwave fully-polarimetric passive observations of the sea surface: A neural network approach," *IEEE Trans. Geosci. Remote Sens.*, vol. 45, no. 7, pp. 2098–2107, Jul. 2007.
[20] L. Pulvirenti, N. Pierdicca, and F. S. Marzano, "Coupling a neural network based forward model and a Bayesian inversion approach to retrieve wind field from spaceborne polarimetric radiometers," *Sensors*, vol. 8, no. 12, pp. 7850–7865, Dec. 2008.
[21] L. Pulvirenti, F. Ticconi, and N. Pierdicca, "Neural network emulation of the integral equation model with multiple scattering," *Sensors*, vol. 9, no. 10, pp. 8109–8125, Oct. 2009.
[22] L. Pulvirenti and N. Pierdicca, "Retrieval of atmospheric and surface parameters from satellite microwave radiometers over the Mediterranean Sea," *IEEE Trans. Geosci. Remote Sens.*, vol. 44, no. 1, pp. 90–101, Jan. 2006.

Luca Pulvirenti (M'07) received the Laurea degree in electronic engineering and the Ph.D. degree in electromagnetism from the Sapienza University of Rome, Rome, Italy, in 1999 and 2004, respectively.

From 2004 to 2009, he was a Postdoctoral Researcher with the Department of Electronic Engineering, Sapienza University of Rome. He is currently a Fixed-Term Researcher with the Department of Information Engineering, Electronics and Telecommunications, Sapienza University of Rome, where, in 2007 and 2008, he taught electromagnetic propagation and presently teaches a course on antennas. His research interests include microwave remote sensing of the atmosphere and the Earth's surface, electromagnetic scattering models of rough surfaces (in particular, bare soil and sea), microwave radiometry of the atmosphere, and inversion of electromagnetic forward models to retrieve soil parameters.

Dr. Pulvirenti is a member of the Italian Society of Electromagnetism (SiEM) and the Italian Association of Remote Sensing (AIT).

Nazzareno Pierdicca (M'04) was born in Rome, Italy, on June 11, 1954. He received the Laurea (Doctor's) degree (*cum laude*) in electronic engineering from the Sapienza University of Rome, Rome, in 1981.

During 1978–1982, he was with the Italian Agency for Alternative Energy (ENEA), where he performed research and development activities in the field of thermal and mechanical behaviors of nuclear fuel rods. From 1982 to 1990, he was with the Remote Sensing Division, Telespazio, Rome. He was involved and was responsible in various projects concerning remote sensing applications, data interpretation, and ground segment design. He was a Principal Investigator of the ESA/JRC Agrisar'86 airborne campaign and a Coinvestigator of the X-SAR/SIR-C experiment. In November 1990, he was with the Department of Electronic Engineering, Sapienza University of Rome. He has been an Investigator of the MAC Europe'91 and X-SAR/SIR-C experiments. He is currently an Associate Professor and teaches remote sensing and antennas with the Faculty of Engineering, Sapienza University of Rome. His research activity mainly concerns electromagnetic scattering models, microwave radiometry of the atmosphere, and SAR land applications.

Prof. Pierdicca is the Chairman of the Geoscience and Remote Sensing Society (Central Italy Chapter).

Frank Silvio Marzano (S'89–M'99–SM'03) received the Laurea degree (*cum laude*) in electrical engineering and the Ph.D. degree in applied electromagnetics from the Sapienza University of Rome, Rome, Italy, in 1988 and 1933, respectively.

In 1993, he collaborated with the Institute of Atmospheric Physics, Consiglio Nazionale delle Ricerche, Rome. From 1994 to 1996, he was with the Italian Space Agency, Rome, as a Postdoctoral Researcher. After being a Lecturer at the University of Perugia, Perugia, Italy, in 1997, he was with the Department of Electrical Engineering and cofounded the Center of Excellence CETEMPS, University of L'Aquila, L'Aquila, Italy, coordinating the Satellite and Radar Remote Sensing Laboratory. In 2005, he was with the Department of Electronic Engineering, Sapienza University of Rome, where he currently teaches courses on antennas and remote sensing. He has published more than 65 papers on international refereed journals and more than 120 extended abstracts in conference proceedings. His current research concerns passive and active remote sensing of the atmosphere from ground-based, airborne, and spaceborne platforms, with a particular focus on precipitation using microwave and infrared data, development of inversion methods, radiative transfer modeling of scattering media, and radar meteorology issues. He is also involved on radio propagation topics in relation to incoherent wave modeling, scintillation prediction, and rain fading analysis along satellite microwave links.

Dr. Marzano is a member of the Italian Society of Electromagnetics (SiEM). Since January 2004, he has been acting as an Associate Editor of IEEE GEOSCIENCE AND REMOTE SENSING LETTERS. In 2004 and 2006, he has been a Co-Guest Editor of the Special Issues on MicroRad for the IEEE TRANSACTIONS ON GEOSCIENCE AND REMOTE SENSING. He was the recipient of the Young Scientist Award of XXIV General Assembly of the International Union of Radio Science (URSI) in 1993. In 1998, he was the recipient of the Alan Berman Publication Award (ARPAD) from the Naval Research Laboratory, Washington, DC. Since 2001, he has been an Italian national delegate for the European COST actions n.720 on atmospheric profiling by ground-based remote sensing and n.280 on satellite fade mitigation techniques.